Progress In Electromagnetics Research, Vol. 115, 191–206, 2011

A NOVEL MOVING TARGET DETECTION APPROACH FOR DUAL-CHANNEL SAR SYSTEM

B. Tian, D.-Y. Zhu, and Z.-D. Zhu

College of Electronics and Information Engineering
Nanjing University of Aeronautics and Astronautics
Nanjing 210016, China

Abstract—A novel approach to moving target detection is proposed for dual-channel SAR system. This approach is on the basis of eigen-decomposition of the sample covariance matrix and examines the statistic of the second eigenvalue and the Along-Track Interferometric (ATI) phase for ground moving target indication. Based on this statistic, a new Constant False Alarm Rate (CFAR) detector can be designed to solve the problem of GMTI. To detect slow moving targets more accurately, the second eigenvalue and the ATI phase pre-thresholds are implemented before a CFAR detector. Experimental results on measured SAR data are presented to demonstrate that this novel detector has wider range of detection velocity and lower false alarm probability.

1. INTRODUCTION

Synthetic Aperture Radar (SAR) [1–5] is a radar imaging technique that generates a map of surface areas and terrain in the range and the cross-range dimension using the radar platform's motion to form the image. Ground Moving Target Indication (GMTI) with SAR has been widely explored for both military and civilian tasks. GMTI is a very difficult problem, due to the difficulty of separating the signal returned from a moving target from the stationary clutter. Techniques for GMTI include the use of single and multi-channel SAR data. Refs. [6–13] take a good overview of them, including multi-looking, Displaced Phase Center Antenna (DPCA), Along Track Interferometry (ATI), mono-pulse processing and signal Space Time Adaptive Processing (STAP).

Received 1 December 2010, Accepted 25 March 2011, Scheduled 29 March 2011
Corresponding author: Bin Tian (tianbin218@163.com).

Along Track Interferometric SAR (AT-InSAR) system is initially introduced to study ocean currents, and then used to detect slow-moving target and estimate their radial velocity. In recent years, some target detectors based on an eigen-decomposition of the dual-channel covariance matrix have been proposed in Refs. [14, 15]. The decomposition elements such as the ATI phase and the second eigenvalue are used as moving target detection metrics. In this paper, a novel metric, which is based on the joint probability density function (PDF) of the ATI phase and the second eigenvalue, is introduced and is applied to detect moving targets. Conventional AT-InSAR systems apply the ATI phase of the SAR image pair to detect moving targets. We propose to consider both the second eigenvalue and the ATI phase information of the SAR images instead of taking only the ATI phase information into account. Experiments on simulated data and measured SAR data will be presented to show that this novel detector has wider range of detection velocity and lower false alarm probability.

The rest of this paper is organized as follows. Section 2 presents a decomposition of the two-channel sample covariance matrix into eigenvalues and a representation of the eigenvectors. Section 3 presents a new metric which combines the second eigenvalue and the ATI phase information. Finally, Section 4 demonstrates the detection capability of the proposed method by measured SAR data.

2. DECOMPOSITION OF THE SAMPLE COVARIANCE MATRIX

Consider an along-track interferometric SAR system with two antennas installed along the flight path. Z_1 denotes the complex SAR image of an imaged area acquired by the first antenna, and Z_2 denotes the complex SAR image of the same area acquired by the second antenna. The two SAR complex images can be modeled as

$$Z_1 = \begin{cases} Z_{c1} + N_1 + Z_{T1} & \text{in presence of moving target} \\ Z_{c1} + N_1 & \text{in absence of moving target} \end{cases}$$

$$Z_2 = \begin{cases} Z_{c2} + N_2 + Z_{T2} & \text{in presence of moving target} \\ Z_{c2} + N_2 & \text{in absence of moving target} \end{cases}$$

where Z_{c1} and Z_{c2} are the clutter processes representing the SAR complex images acquired from two antennas; N_1 and N_2 are due to the presence of thermal noises at the receivers; Z_{T1} and Z_{T2} denote the SAR images of the moving targets.

If the two channel samples are collocated as a vector

$$\vec{\mathbf{Z}}(k) = \begin{bmatrix} Z_1(k) \\ Z_2(k) \end{bmatrix} \tag{1}$$

the sample covariance matrix between two zero-mean complex Gaussian signals can be defined as

$$\widehat{\mathbf{R}} = \frac{1}{n}\sum_{k=1}^{n} \vec{\mathbf{Z}}(k)\vec{\mathbf{Z}}^{\mathrm{H}}(k) \tag{2}$$

where H denotes Hermitian transpose, n is the effective number of looks. The eigen-decomposition of the sample covariance matrix can be given by

$$\widehat{\mathbf{R}} = \frac{1}{n}\sum_{k=1}^{n} \vec{\mathbf{Z}}(k)\vec{\mathbf{Z}}^{\mathrm{H}}(k) = \begin{bmatrix} \widehat{R}_{11} & \widehat{R}_{12} \\ \widehat{R}_{21} & \widehat{R}_{22} \end{bmatrix} = \mathbf{U}\begin{bmatrix} \Lambda_1 & 0 \\ 0 & \Lambda_2 \end{bmatrix}\mathbf{U}^{\mathrm{H}} \tag{3}$$

where Λ_1 and Λ_2 represent the two eigenvalues of $\widehat{\mathbf{R}}$ respectively, the columns of $\mathbf{U}$ are the corresponding eigenvectors. It shows that one of possible representations for $\mathbf{U}$ can be written as

$$\mathbf{U} = \begin{bmatrix} \cos\Theta & e^{j\Delta}\sin\Theta \\ e^{-j\Delta}\sin\Theta & -\cos\Theta \end{bmatrix} \tag{4}$$

After expending $\mathbf{U}^{\mathrm{H}}\widehat{\mathbf{R}}\mathbf{U}$, we can find that

$$\Delta = \arg(\widehat{R}_{12}), \quad \text{and} \tag{5}$$

$$\Theta = \begin{cases} \frac{1}{2}\arctan\left(\frac{2\left|\widehat{R}_{12}\right|}{\widehat{R}_{11}-\widehat{R}_{22}}\right) & \widehat{R}_{11} \geq \widehat{R}_{22} \\ \frac{1}{2}\arctan\left(\frac{2\left|\widehat{R}_{12}\right|}{\widehat{R}_{11}-\widehat{R}_{22}}\right) + \frac{\pi}{2} & \widehat{R}_{11} < \widehat{R}_{22} \end{cases} \tag{6}$$

$$\Lambda_1 = \frac{1}{2}\left[\widehat{R}_{11} + \widehat{R}_{22} + \sqrt{4\left|\widehat{R}_{12}\right|^2 + (\widehat{R}_{11}-\widehat{R}_{22})^2}\right] \tag{7}$$

$$\Lambda_2 = \frac{1}{2}\left[\widehat{R}_{11} + \widehat{R}_{22} - \sqrt{4\left|\widehat{R}_{12}\right|^2 + (\widehat{R}_{11}-\widehat{R}_{22})^2}\right] \tag{8}$$

The random phase Δ is commonly referred to the ATI phase. The random variable Θ is named after the similarity. It measures the degree of similarity between the two channels, and behaves like the cross-correlation coefficient. It has been demonstrated in Refs. [14, 15] that Δ, Θ and Λ_2 could be considered as GMTI metrics. However, it turns out that although Θ has a response to moving targets, its degree of sensitivity to moving targets is comparatively lower.

3. INTEGRATION OF THE SECOND EIGENVALUE AND THE ATI PHASE TO A NOVEL GMTI METRIC

In this section, based on the joint PDF of the second eigenvalue and the ATI phase, we now introduce a new metric that joints the second eigenvalue and the ATI phase information together. First of all, the joint PDF of the second eigenvalue and the ATI phase is presented.

3.1. The Probability Density Function of the Second Eigenvalue and the ATI Phase

When it is assumed that the two channels are balanced in power (i.e., that the diagonal elements of the covariance matrix are equal), the joint probability density function of the eigenvalues and eigenvectors can be computed in [15] and is given by

$$\begin{aligned} & f_{\Lambda_1,\Lambda_2,\Delta,\Theta}(\lambda_1,\lambda_2,\phi,\theta) \\ =& \frac{\sin 2\theta(\lambda_1\lambda_2)^{n-2}(\lambda_1-\lambda_2)^2}{2\pi\Gamma(n)\Gamma(n-1)\det(\mathbf{R})^n} e^{Tr\left(-\mathbf{U}^H\mathbf{R}^{-1}\mathbf{U}\begin{bmatrix}\lambda_1 & 0\\ 0 & \lambda_2\end{bmatrix}\right)} \end{aligned} \tag{9}$$

where $\mathbf{R}$ denotes the clutter covariance matrix. $\Gamma(n)$ is an gamma function. $Tr(\cdot)$ stands for exponential trace. $\det(\cdot)$ denotes the determinant operator. Domain limits are $0 < \lambda_2 < \lambda_1 < \infty, \varphi \in [-\pi,\pi)$, and $\theta \in [0,\pi/2)$.

Integration conducted over Λ_1 and Θ respectively will lead to the marginal probability distribution of Δ and Λ_2. The joint PDF of Δ and Λ_2 can be calculated in [15] with the result

$$\begin{aligned} f_{\Lambda_2,\Delta}(\lambda_2,\varphi) =& \frac{\lambda_2^{n-2}}{2\pi\Gamma(n)\Gamma(n-1)(s_1s_2)^n}\int_0^{\pi/2}\sin(2\theta)e^{-B\lambda_2}\left[\frac{\Gamma(n+1,A\lambda_2)}{A^{n+1}}\right. \\ & \left. -\frac{2\lambda_2\Gamma(n,A\lambda_2)}{A^n}+\frac{\lambda_2^2\Gamma(n-1,A\lambda_2)}{A^{n-1}}\right]d\theta \end{aligned} \tag{10}$$

where

$$\begin{cases} A = \frac{(s_1+s_2)-(s_1-s_2)\cos\varphi\sin(2\theta)}{2s_1s_2} \\ B = \frac{(s_1+s_2)+(s_1-s_2)\cos\varphi\sin(2\theta)}{2s_1s_2} \end{cases} \tag{11}$$

$\Gamma(n,z)$ is an incomplete gamma function and $s_1 > s_2$ represent the two eigenvalues of $\mathbf{R}$ respectively. The joint PDF of Δ and Λ_2 is reported in Fig. 1 for $s_1 = 1.921$, $s_2 = 0.079$, $n = 2$.

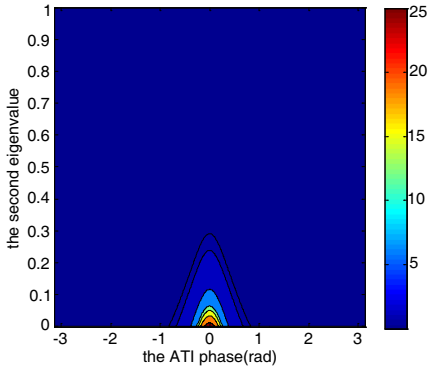

Figure 1. The joint PDF of the second eigenvalue and the ATI phase with $s_1 = 1.921$, $s_2 = 0.079$, $n = 2$.

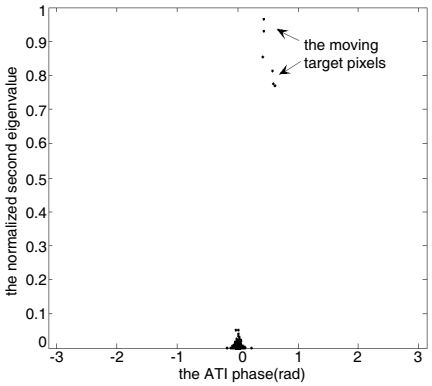

Figure 2. The phase deviations of the phase difference of each pixel against the normalized second eigenvalue of the pixel in the absence of any noise with SCR = 7.6 dB and 9.5 dB respectively.

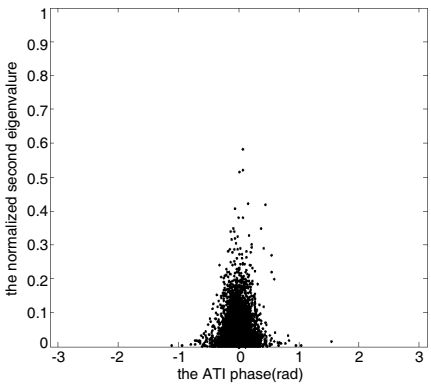

Figure 3. The phase deviations of the phase difference of each pixel against the normalized second eigenvalue of the pixel in the presence of the noise with CNR = 12.1 dB.

3.2. A Novel Detector Based on the Combination of the Second Eigenvalue and the ATI Phase

In Fig. 2, we have plotted the phase deviations of the phase difference of each pixel against the normalized second eigenvalue of the pixel in the absence of any noise. The pixels consist of the moving targets pixels and the clutter pixels. The parameters are that the signals to clutter ratio (SCR) are 7.6 dB and 9.5 dB respectively. As is seen from

Fig. 2, the clutter pixels in the absence of any noise mainly concentrate around the coordinate origin. That is to say, the phase difference of the clutter pixels gets close to zero and the normalized second eigenvalues are small. For the moving targets pixels, the deviations of the phase difference would be far away from zero and the normalized second eigenvalues are much larger. Here we can set a phase threshold Δ_{th} or an eigenvalue threshold Λ_{th} to reliably detect the moving targets. Δ_{th} and Λ_{th} can be computed with the following expressions

$$\begin{aligned} & 2\int_{\Delta_{th}}^{\pi} f_{\Delta}(\zeta|\, n,\gamma)d\zeta \\ = & \int_{\Delta_{th}}^{\pi} (1-\gamma^2)^n \sin(2\zeta)\left[2n_2F_1(1+n,1/2;1;\gamma^2\sin^2(2\zeta))\right. \\ & \left.+(1-2n)_2F_1(n,1/2;1;\gamma^2\sin^2(2\zeta))\right]d\zeta = \phi_{\Delta} \end{aligned} \tag{12}$$

$$\begin{aligned} & \int_{\Lambda_{th}}^{+\infty} f_{\Lambda_2}(\xi|\, n,s_1,s_2)d\xi \\ = & \int_{\Lambda_{th}}^{+\infty} \frac{(\xi/s_2)e^{-\xi/s_2}\Gamma(n,\xi/s_2)}{\Gamma(n)\Gamma(n-1)(s_1-s_2)}\left(\frac{s_1}{s_2}-\frac{\xi/s_2}{n-1}\right) \\ & -\frac{(\xi/s_1)e^{-\xi/s_1}\Gamma(n,\xi/s_1)}{\Gamma(n)\Gamma(n-1)(s_1-s_2)}\left(\frac{s_2}{s_1}-\frac{\xi/s_1}{n-1}\right)d\xi = \phi_{\Lambda_2} \end{aligned} \tag{13}$$

where f_{Δ} denotes the PDF of the ATI phase in the absence of the moving targets. γ stands for the clutter coherence. f_{Λ_2} denotes for the PDF of the second eigenvalue in the absence of the moving targets. ϕ_{Λ_2} and ϕ_{Δ} stand for false alarm probability.

However, actually, all pixels often contain phase noise and the high noise. Consequently, it brings about some difficulty to SAR system for detecting moving targets. The parameters are that the clutter o noise ratio (CNR) is 12.1 dB. Fig. 3 provides the phase deviations of the phase difference of each pixel against the normalized second eigenvalue of the pixel in the presence of the noise. In Fig. 3, because of the influence of the noise, both the phase deviations and the second eigenvalues of lots of pixels increase in varying degrees. In this case, the performance of the detection process would be not so well if we continue to utilize Δ or Λ_2 to detect moving targets. As is learned from the eigen-decomposition of the sample covariance matrix, Λ_2 takes advantage of changes in the amplitude information of the elements of the sample covariance matrix to detect moving targets, while Δ utilizes changes in the phase information of the elements ($\widehat{R}_{12}$ or $\widehat{R}_{21}$) of the sample covariance matrix to detect moving targets. To make full use of the amplitude and phase information of the elements of the sample

covariance matrix, we examine the statistic of Δ or Λ_2 for ground moving target indication. Fig. 4 plots a set of contour lines of the joint PDF of the second eigenvalue and the ATI phase on the Fig. 3. The value of the contour lines increases from the outside to the inside. The larger the value of the contour line, the greater the probability that the pixel falls near this contour line. As is seen from the Fig. 4, we can find out a contour line (the outermost contour line in the Fig. 4) which contains most of the clutter pixels. That is to say, it would reliably detect the moving targets if this contour line is set to be the envelope threshold.

The envelope threshold's value in Fig. 4 can be calculated in the following way. It is assumed that ξ_{Λ_2} and ζ_Δ are the second eigenvalue and the ATI phase of the clutter pixel respectively. $T_{\Lambda_2,\Delta}$ denotes the contour line's value corresponding to the envelope threshold. $\phi_{\Lambda_2,\Delta}$ stands for false alarm probability. Under these assumptions, $T_{\Lambda_2,\Delta}$ can be given by

$$P\left\{f_{\Lambda_2,\Delta}(\xi_{\Lambda_2},\zeta_\Delta) < T_{\Lambda_2,\Delta}\right\} = \phi_{\Lambda_2,\Delta} \tag{14}$$

where $f_{\Lambda_2,\Delta}$ denotes for the joint PDF of Δ and Λ_2 given by Equation (10). After completing the calculation of the envelope threshold $T_{\Lambda_2,\Delta}$, we can utilize this threshold to detect moving targets. The detection process is comprised of the following three steps: In step

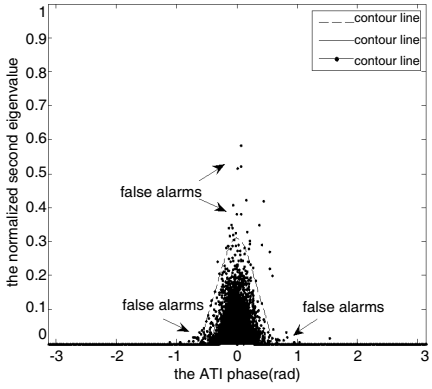

Figure 4. The phase deviations of the phase difference of each pixel against the normalized second eigenvalue of the pixel and a set of contour lines of the joint PDF of the second eigenvalue and the ATI phase.

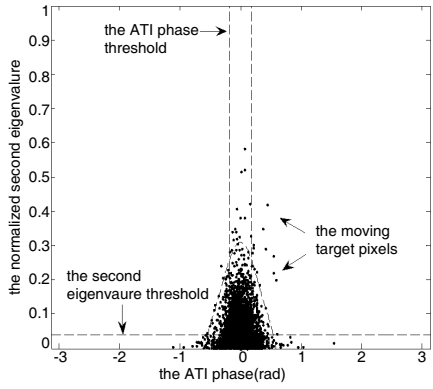

Figure 5. The envelope threshold, the ATI phase and the second eigenvalue pre-thresholds.

1, the ATI phase Δ_i and the second eigenvalue $\Lambda_{2/i}$ of each pixel are computed by Equations (5) and (8). In step 2, Δ_i and $\Lambda_{2/i}$ computed by the first step are substituted into Equation (10) and calculate the likelihood function value $f_{\Lambda_2,\Delta}(\Lambda_{2/i}, \Delta_i)$ of each pixel. In step 3, the size of $T_{\Lambda_2,\Delta}$ and $f_{\Lambda_2,\Delta}(\Lambda_{2/i}, \Delta_i)$ is compared. If $f_{\Lambda_2,\Delta}(\Lambda_{2/i}, \Delta_i)$ is larger than or equal to $T_{\Lambda_2,\Delta}$, it is judged that this pixel is the clutter one. Otherwise, it is the moving target pixel.

It is also found in the Fig. 4 that not all of the pixels out of the envelope threshold are the moving target pixels and include some false alarms. Those false alarms result from the noise and the clutter with strong power. We can set a fair ATI phase and the second eigenvalue pre-thresholds to eliminate those false alarms respectively. The ATI phase and the second eigenvalue pre-thresholds are computed in Section 4. Fig. 5 shows the envelope threshold, the ATI phase and the second eigenvalue pre-thresholds.

In above simulation experiments, the algorithm for moving target indication concentrates on targets with only radial velocity. In this paragraph, targets with both radial velocity and along-track velocity are considered. Fig. 6 plots the phase deviations of the phase difference of each pixel against the normalized second eigenvalue of the pixel in the case of targets with both radial velocity and along-track velocity for $v_a = 1.6\,\mathrm{m/s}$. From the Fig. 6, we see that the ATI phase and the second eigenvalue of the moving target pixels become smaller. The reason for this phenomenon is that the targets with along-track velocity are defocused and smeared, i.e., their energy is spread over an

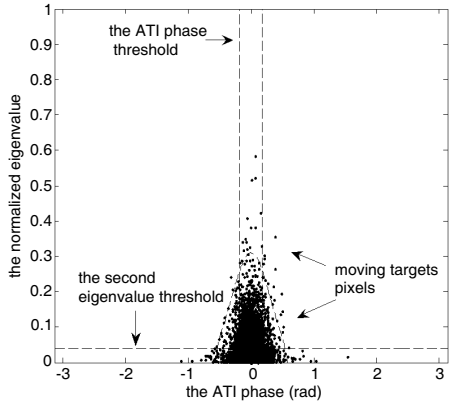

Figure 6. The phase deviations of the phase difference of each pixel against the normalized second eigenvalue of the pixel in the case of targets with both radial velocity and along-track velocity.

Table 1. Radar system operating parameters.

Radar system operating parameters	Value
Total bandwidth	180 MHz
Airplane velocity	110 m/s
Pulse repetion frequency	1250 Hz
Number of pulse per coherence pulse interval	1024
Baseline	0.35 m
Scene center range at aperture center	24000 m
Altitude	5300 m
Frequency band	X-band frequency

extended area. This leads to a diminution in the signal to the clutter ratio (SCR). As the along-track speed increases, moving targets will be more seriously blurred. Consequently, the SCR would become much lower, and it would bring about some challenges for ground moving target indication.

4. MEASURED SAR DATA ANALYSIS

The proposed detector applied to the measured SAR data is presented in this section. Real data are collected by an airplane. An AT-InSAR system with three channels is configured in this airplane, working at X-band in side-looking mode. Radar system operating parameters are addressed in Tab. 1. The imaged area includes a stretch of road. There are five moving tested vehicles and several fixed corner reflectors on the road. The moving direction of three vehicles among them is contrary to that of the other two. Their velocity is between 1 m/s and 7 m/s. The entire signal processing chain for Moving Target Detection (MTD) is schematically shown in the flow-chat of Fig. 7.

4.1. Image Registration and Calibration of Array Errors

Due to the raw data acquired from the different antennas, it is necessary to implement a co-registration between the two SAR images before the detection. The image registration procedure mentioned in Ref. [16] is applied at the SAR data processing stage. In addition, the two channels are often mismatched in the amplitude and phase responses because the antenna patterns of different sensors would not be identical. Those mismatches between different receiving channels can be equalized by exploiting the received data themselves. Several methods have been proposed for calibrating various kinds of errors in

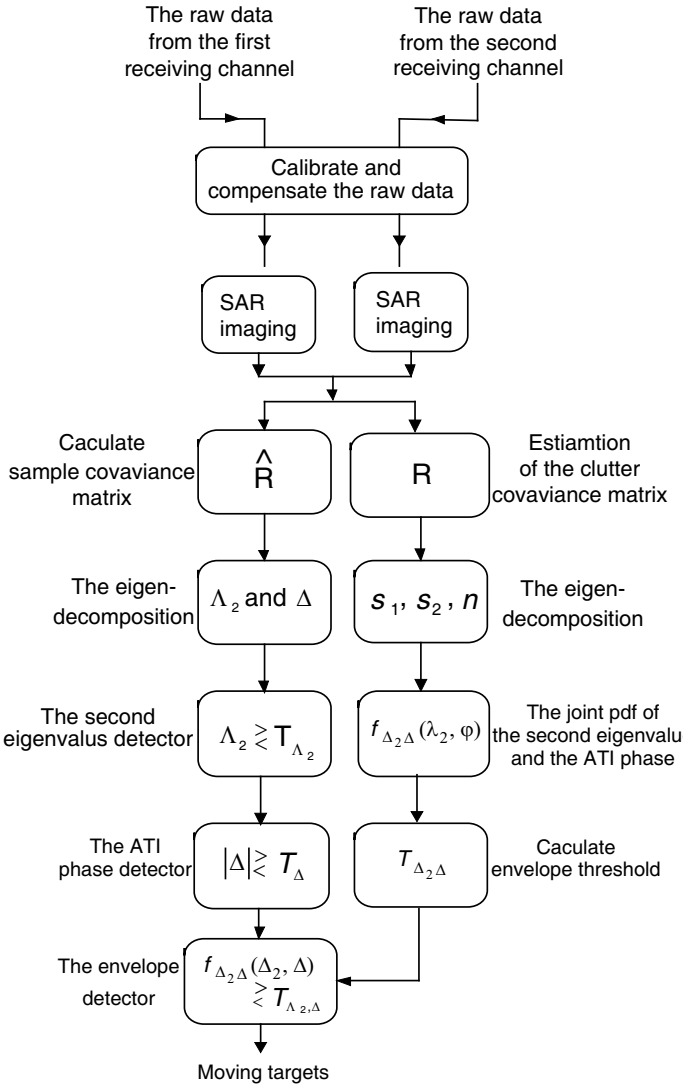

Figure 7. Flow-chart of the MTD signal processing chain.

different domains (see Refs. [17, 18]). In our experiment, we adopt the approach mentioned in Ref. [18] to calibrate the array errors in two dimension frequency domain. Fig. 8 provides the amplitude and phase responses of the two-channel SAR system before and after applying calibration of array errors for comparison. All the response curves are normalized with respect to that of channel 2.

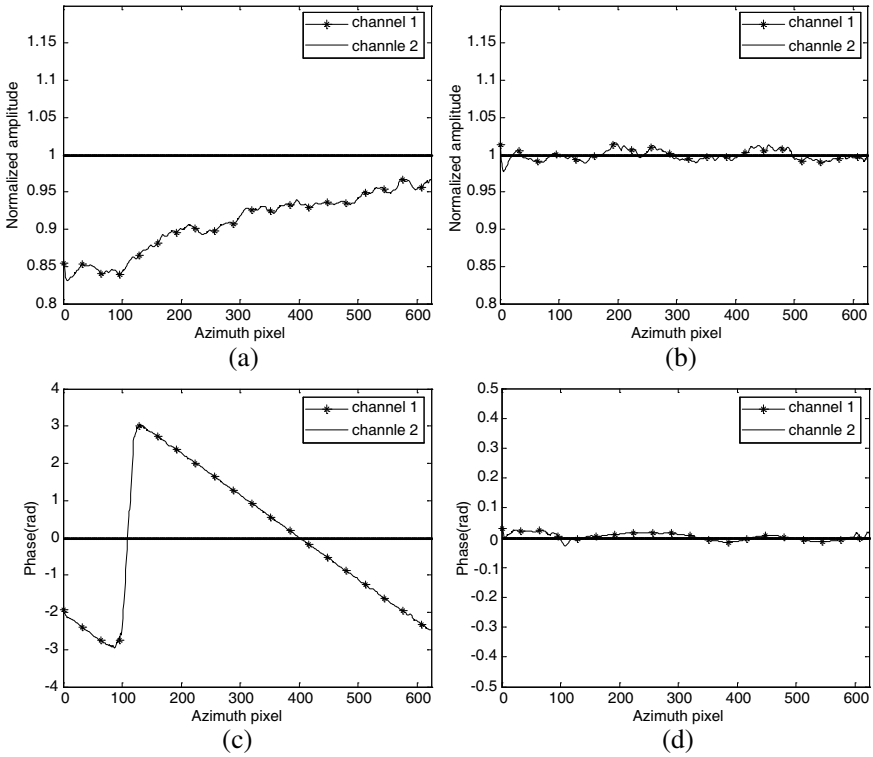

Figure 8. Array responses before and after calibration of array errors. (a) Amplitude responses before calibration of array errors. (b) Amplitude responses after calibration of array errors. (c) Phase responses before calibration of array errors. (d) Phase responses after calibration of array errors.

After completing the calibration of array errors, we apply polar format algorithm [19–23] to measured SAR data. Figs. 9(a) and (b) provide SAR images of the tested site acquired by the first antenna and the second one respectively. As is seen in Fig. 9(a), there are only corner reflectors on the road. The tested vehicles deviate from the road in the SAR image due to the presence of their radial velocity.

4.2. Parameter Estimation

All necessary parameters need to be estimated directly from measured SAR data before the implementation of a CFAR detector. Those parameters include the sample covariance matrix, the clutter covariance matrix, the effective number of looks, the ATI phase and

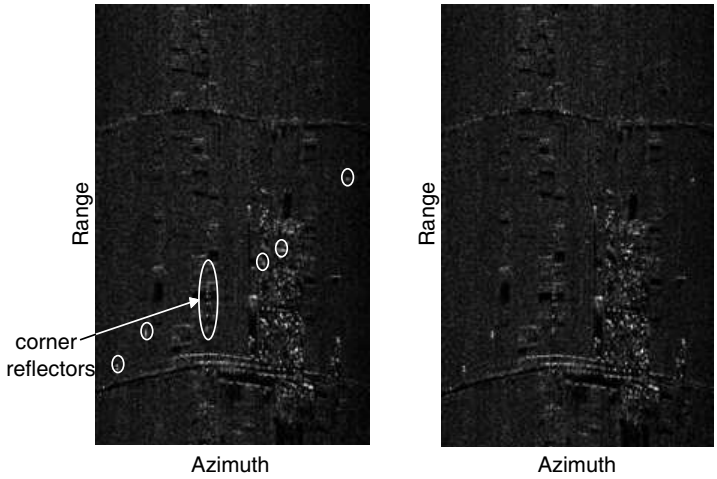

Figure 9. SAR images of the tested site: (a) SAR image of the tested site acquired by the first antenna. (b) SAR image of the tested site acquired by the second antenna.

the second eigenvalue pre-thresholds. Estimation procedures of the clutter covariance matrix and the effective number of looks have been discussed in great detail [12]. Taking the limited space into consideration, we mainly introduce how to estimate sample covariance matrix and the ATI phase and the second eigenvalue pre-thresholds as follows.

4.2.1. The Sample Covariance Matrix

In practice, the sample covariance matrix is often computed by using the neighboring pixels. Assuming that neighboring pixels are independent identical distribution (i.i.d), the sample covariance matrix $\widehat{\mathbf{R}}(x,y)$($x$ and y refer to the azimuth and range indexes in SAR image) can be specified as

$$\widehat{\mathbf{R}}(x,y) = \frac{1}{M \times N} \sum_{i=-\frac{M-1}{2}}^{\frac{M-1}{2}} \sum_{j=-\frac{N-1}{2}}^{\frac{N-1}{2}} \mathbf{Z}(x+i,y+j)\mathbf{Z}(x+i,y+j)^{\mathrm{H}} \quad (15)$$

where $\mathbf{Z}(x,y) = [Z_1(x,y), Z_2(x,y)]^{\mathrm{T}}$, $M \times N$ is the number of pixels in the covariance estimation. As is learned from Ref. [12], the effective number of looks has close relationship with the number of pixels. The larger the number of pixels in the covariance estimation is, the larger

the effective number of looks is. When the chosen effective number of looks is much larger, the "speckle noise" could be reduced effectively, and false alarms generated by the impact of noise in the resulting detection will get smaller. Unfortunately, the large effective number of looks is at the expense of azimuth and range resolutions. For this reason, a tradeoff between the effective number of looks and resolutions has to be considered in choosing the number of pixels in the covariance estimation. In this paper, we choose $M \times N = 7 \times 7$.

4.2.2. The ATI Phase and the Second Eigenvalue Pre-thresholds

It is assumed that $\Lambda_{2/i}$ denotes the second eigenvalue of the ith pixel. N is the total number of the pixels. δ_Δ is the standard deviation of the ATI phase of all the pixels. The ATI phase pre-threshold T_Δ and the second eigenvalue pre-threshold T_Δ can be computed with the following expressions:

$$\left.\begin{array}{l} T_{\Lambda_2} = k_1 \frac{1}{N} \sum\limits_{i=1}^{N} \Lambda_{2/i} \\ T_\Delta = k_2 \delta_\Delta \end{array}\right\} \tag{16}$$

where k_1 and k_2 are two adjustable coefficients. Domain limits are $1 \leq k_1 \leq 2.5$, $1 \leq k_2 \leq 1.5$. When the value of k_1 is too large, the moving targets with weak power would be undetected. The minimum detectable velocity of the moving target would increase when the value of k_2 is large. In measured data processing, both k_1 and k_2 are set to 1.

4.3. CFAR Detector

Using estimation procedures above, the envelope threshold can be computed for a given false alarm rate (5×10^{-4}). This threshold is then applied to the computed metric. Fig. 10(a) illustrates the resulting detection of moving targets with the proposed detector. As is seen in the Fig. 10(a), nine targets are detected in total. Those targets marked with the sequence number are the correct moving targets (the 1–5th moving targets are tested vehicles) after our confirmation, and the others are false alarms. For comparative purpose, we apply the approaches using the ATI phase and the second eigenvalue to the measured SAR data for the same false alarm rate respectively. Figs. 10(b) and (c) show the resulting detection of moving targets with the ATI phase detector and the second eigenvalue detector respectively. Comparing three different strategies in terms of the resulting detection, it is easily found that both the proposed detector and the second eigenvalue detector can find all the tested vehicles in this measured

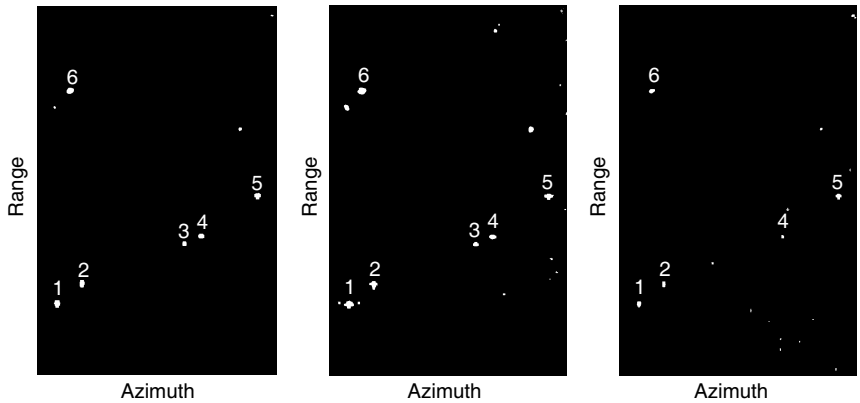

Figure 10. SAR images of the resulting detection: (a) The resulting detection with the proposed detector for a given constant false alarm rate. (b) The resulting detection with the second eigenvalue detector for a given constant false alarm rate. (c) The resulting detection with the ATI detector for a given constant false alarm rate.

SAR data. However, the difference between two strategies is that the number of false alarms with the second eigenvalue detector is larger than that using the proposed detector. That is to say, the performance of detection with the proposed detector is better than that of detection with the second eigenvalue detector under the same condition. The ATI phase detector finds only five moving targets. Meanwhile, there are also some false alarms in the SAR image of the resulting detection. The reason for not detecting the 3th moving target is that the speed of this target is too small.

5. CONCLUSION

This paper has presented and investigated a novel detector for the indication of ground moving targets for the two-channel SAR-GMTI, which is on the basis of eigen-decomposition of the sample covariance matrix and combines the ATI phase and the second eigenvalue information. Experimental results on simulation data and measured SAR data have been presented to show and to validate that compared with the ATI phase detector and the second eigenvalue detector, the proposed detector shows better performance of moving target detection.

ACKNOWLEDGMENT

Supported by the National Natural Science Foundation of China (No. 61071165) and China Postdoctoral Foundation (No. 20090461119).

REFERENCES

1. Zhang, Y.-D., L. Wu, and G. Wei, "A new classifier for polarimetric SAR images," *Progress In Electromagnetics Research*, Vol. 94, 83–104, 2009.
2. Chua, M. Y. and V. C. Koo, "FPGA-based chirp generator for high resolution UAV SAR," *Progress In Electromagnetics Research*, Vol. 99, 71–88, 2009.
3. Sun, J., S. Mao, G. Wang, and W. Hong, "Extended exact transfer function algorithm for bistatic SAR of translational invariant case," *Progress In Electromagnetics Research*, Vol. 99, 89–108, 2009.
4. Sun, J., S. Mao, G. Wang, and W. Hong, "Polar format algorithm for spotlight bistatic SAR with arbitrary geometry configuration," *Progress In Electromagnetics Research*, Vol. 103, 323–338, 2010.
5. Zhao, Y. W., M. Zhang, and H. Chen, "An efficient ocean SAR raw signal simulation by employing fast fourier transform," *Journal of Electromagnetic Waves and Applications*, Vol. 24, No. 16, 2273–2284, 2010.
6. Raney, R. K., "Synthetic aperture imaging radar and moving targets," *IEEE Transactions on Aerospace and Electronic Systems*, Vol. 7, No. 3, 499–505, May 1971.
7. Zhang, L., H.-D. Guo, and C.-M. Han, "Moving targets detection in SAR images based on sub-aperture decomposition," *Acta Electronica Sinica*, Vol. 36, No. 6, 1210–1213, 2008.
8. Soumekh, M., "Moving target detection and imaging using an X-band along-track monopulse SAR," *IEEE Transactions on Aerospace and Electronic Systems*, Vol. 38, No. 1, 315–333, 2002.
9. Nohara, T. J. and P. Weber, "SAR-GMIT processing with Canada's radarsat2 satellite," *Adaptive System for Signal Processing, Communications, and Control Symposium*, 379–384, Lake Louise, Alta, October 1–4, 2000.
10. Pascazio, V., G. Schirinzi, and A. Farina, "Moving target detection by along-track interferometry," *Geoscience and Remote Sensing Symposium*, 3024–3026, Sydney, NSW, July 9–13, 2001.
11. Chapin, E. and C. W. Chen, "Airborne along-track interferometry

for GMTI," *IEEE Transactions on Aerospace and Electronic Systems*, Vol. 24, No. 5, 13–18, 2009.

12. Gierull, C. H., "Statistics of SAR interferograms with application to moving target detection," *Technical Report TR 2001-045, Defence Research and Development*, 26–40, Canada, July 2001.
13. Gong, Q. and Z. -D. Zhu, "Study stap algorithm on interference target detect under non-homogenous environment," *Progress In Electromagnetics Research*, Vol. 99, 211–224, 2009.
14. Sikaneta, I., C. Gierull, and J. Y. Houinard, "Metrics for SAR-GMTI based on eigen-decomposition of the sample covariance matrix," *IEEE National Radar Conference*, 442–477, Adelaide, Australia, September 3–5, 2003.
15. Sikaneta, I. C. and J. Y. Houinard, "Eigen-decomposition of the multi-channel covariance matrix with applications to SAR-GMTI," *IET Signal Processing*, 1501–1535, Vol. 84, No. 9, 2004.
16. Fornaro, G. and G. Franceschetti, "Image registration in interferometric SAR processing," *IEE Proc. — Radar, Sonar Navig.*, Vol. 142, No. 6, 313–320, 1995.
17. Soumekh, M., "Signal subspace fusion of uncalibrated sensors with application in SAR and diagnostic medicine," *IEEE Transactions on Image Processing*, Vol. 8, No. 1, 127–137, 1999.
18. Ender, J. H. G., "The airborne experimental multi-channel SAR system AER-II," *EUSAR Conf. Proceedings*, 49–52, Königswinter, Germany, 1996.
19. Zhu, D., S. Ye, and Z. Zhu, "Polar format agorithm using chirp scaling for spotlight SAR image formation," *IEEE Transactions on Aerospace and Electronic Systems*, Vol. 44, No. 4, 1433–1448, 2008.
20. Nie, X., D.-Y. Zhu, and Z.-D. Zhu, "Application of synthetic bandwidth approach in SAR polar format algorithm using the deramp technique," *Progress In Electromagnetics Research*, Vol. 80, 447–460, 2008.
21. Mao, X., D.-Y. Zhu, and Z.-D. Zhu, "Signatures of moving target in polar format spotlight SAR image," *Progress In Electromagnetics Research*, Vol. 92, 47–64, 2009.
22. Mao, X., D.-Y. Zhu, L. Wang, and Z.-D. Zhu, "Comparative study of RMA and PFA on their responses to moving target," *Progress In Electromagnetics Research*, Vol. 110, 103–124, 2010.
23. Wang, X., D.-Y. Zhu, and Z.-D. Zhu, "An Implementation of bistatic PFA using chirp scaling," *Journal of Electromagnetic Waves and Applications*, Vol. 24, No. 5–6, 745–753, 2010.